Multi-Band Plasmonic Platform Utilizing UT-Shaped Graphene Antenna Arrays

Multi-Band Plasmonic Platform Utilizing UT-Shaped Graphene Antenna Arrays

Yasa Ekşioğlu,[†,*] Arif E. Cetin,[‡] Habibe Durmaz[§]

[†]*Department of Electrical and Electronics Engineering, Istanbul Kemerburgaz University, Mahmutbey Dilmenler Caddesi, No: 26, 34217 Bağcılar Istanbul, Turkey.*

[‡]*Koch Institute for Integrative Cancer Research, Massachusetts Institute of Technology, Cambridge, MA 02139, USA.*

[§]*Department of Electrical and Electronics Engineering, Recep Tayyip Erdoğan University Zihni Derin Yerleşkesi, Fener Mahallesi 53100 Rize, Turkey*

*Corresponding author: yasa.eksioglu@kemerburgaz.edu.tr

ABSTRACT

In this work, we introduce a plasmonic platform based on UT-shaped graphene antenna arrays. The proposed multi-resonant platform shows three different resonances, which can be independently tuned. The physical origin of these modes is shown with FDTD near-field distribution analyses, which are used to statically tune each resonance wavelength via the geometrical parameters, corresponding to different near-field localization. We achieve statistical tuning of multiple resonances also by changing the number of graphene layers. Another static tuning of the optical response of the UT-shaped graphene antenna is achieved via the chemical potential and the relaxation time.

KEYWORDS: Surface plasmon, graphene plasmonics, multi-band

INTRODUCTION

Surface plasmons (SPs) are the collective electron oscillations, propagating at an interface between a metal and a dielectric. The confinement of light through these surface waves with large near-field intensity enhancements [1–3] enables various applications, i.e., surface-enhanced vibrational spectroscopy [4–6], label-free biosensing [7–8] and high-efficiency photovoltaics [9]. Recently, graphene has been utilized in

plasmonics due to its metallic behavior at mid- to far-IR spectral range such that it can control, confine, and manipulate light through SP excitation [10-13]. In that sense, collective oscillations of the electrons (or hole) gas in two-dimensional graphene sheets can produce guided electromagnetic waves with strong sub-wavelength confinement. Plasmonic resonances occur at mid-infrared and terahertz frequencies for typical carrier densities (several 10^{12} cm^{-2}) of graphene as opposed to visible or near-infrared excitations of traditional metallic plasmonic structures. As a result of these favorable properties, graphene plasmons covering mid- to far-IR frequency ranges have been extensively used in theoretical and experimental studies [13-24]. In addition, several device applications have been reported, including optoelectronic devices [14], ultrafast transistor based photodetectors [25-27], optical modulators [28,29], light emitters [30,31] transparent solar cells [32], and biosensors [33, 34].

In this work, we introduce a plasmonic platform based on multi-resonant UT-shaped graphene plasmonic antenna arrays as shown in Figure 1. The platform supports 3 distinct plasmonic resonances in the THz frequency range. The resonance frequencies depend on the geometrical device parameters, chemical potential, relaxation time, number of graphene layers, which are extensively investigated by finite-difference time-domain (FDTD) simulations. The paper is organized as follows: In Methods section, we explain the conductivity relation in graphene and express its plasmonic behavior in terms of conductivity. In Results section, we introduce the UT-shaped graphene antenna system on a thin SiN film. The effect of geometrical parameters on the spectral position of each plasmonic resonance is investigated in detail. The physical origin of each plasmonic mode is shown in nearfield analyses with FDTD simulations. The effect of chemical potential, relaxation time and the number of the graphene layers on the multi-band response is investigated. Such graphene geometry can be experimentally achieved by Electron Beam Lithography (EBL) based nano-fabrication techniques. In this paper, we theoretically investigate the multi-band behavior and experimental characterization of the system will be demonstrated later. Commercial graphene grown by chemical vapor deposition (CVD) on copper foil can be used to have a large continuous sheet of graphene. First, poly(methyl methacrylate) (PMMA) is covered onto graphene on copper foil in order to prepare a supporting layer film. Then, the copper foil is etched away with copper etchant to have a free-standing graphene layer, which is floating on the surface of copper etchant. By using a SiN substrate, this floating sheet of graphene is fished out on top of the substrate with a following acetone bath to remove PMMA and a dry annealing process. After obtaining a large continuous sheet of graphene layer, EBL is implemented in order to pattern the UT-shaped antennas, which followed by plasma ashing to etch away the graphene outside of the UT-shape. Finally, the acetone bath and another annealing process is applied to clean out any undesired residue.

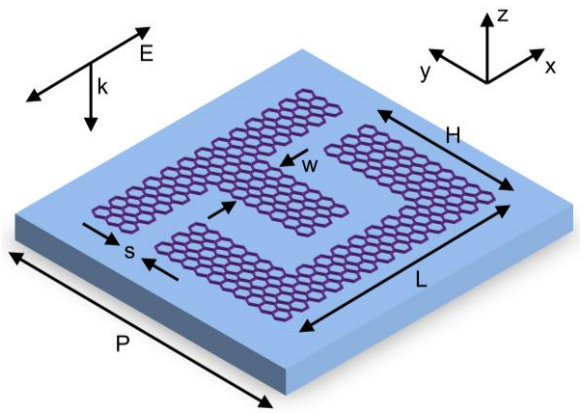

Figure 1. Schematic view of the UT-shaped graphene antenna. The geometrical device parameters are H (height), L (length), w (rod width), s (distance between U- and T-antennas) and P is the period of the antenna array. The graphene structure stands on a SiN (silicon nitride) substrate (denoted with blue).

METHODS

The linear response theory investigates the dynamic behavior of a condensed-matter system at thermal equilibrium in the presence of a small external field. The response of the system is expressed by Kubo formula [34-38]. If an external electric field is applied, the response of the system and the linear response coefficient are represented by current and conductivity, respectively. The optical response of graphene is determined by its conductivity where the relaxation time ($\boldsymbol{\tau = \mu_c \mu / e v_F^2}$, $\boldsymbol{\mu_c = \hbar v_f \sqrt{\pi n}}$, $\boldsymbol{v_F = 10^6\, m/s}$, $\boldsymbol{\mu_c}$ is the chemical potential, $\boldsymbol{e}$ is the elementary charge, $\boldsymbol{\mu}$ is the carrier mobility of the electrons in graphene which is less than the frequency applied ($\boldsymbol{\tau^{-1} \ll \hbar\omega}$, $\boldsymbol{\omega}$ is the frequency, $\hbar$ is the reduced Planck constant) and $\boldsymbol{n}$ is the carrier density [39]. From these relations, carrier density can be calculated as $\boldsymbol{n = (e^2 v_F^2 \tau^2)/(\pi \mu_c^2 \hbar^2)}$. For a given chemical potential of $\boldsymbol{\mu_c = 0.4\ and\ \tau = 0.5\ ps}$, the carrier density is $\boldsymbol{n}$ = 1.47×10^{13} cm^{-2}, where mobility of the graphene is chosen as 10000cm^2/Vs from the [40]. According to graphene's semiconducting characteristics, conductivity of graphene that consists of inter- and intra-band transitions ($\boldsymbol{\sigma = \sigma_{intra} + \sigma_{inter}}$) [38] is mainly controlled by the electron-hole excitations. The corresponding conductivity of graphene is written as:

(Equation-1)

$$\boldsymbol{\sigma(\omega) = \frac{e^2 \omega}{i\pi\hbar}\left[\int_{-\infty}^{+\infty} d\varepsilon \frac{|\varepsilon|}{\omega^2}\frac{df_0(\varepsilon)}{d\varepsilon} - \int_0^{+\infty} d\varepsilon \frac{f_0(-\varepsilon) - f_0(\varepsilon)}{(\omega + i\delta)^2 - 4\varepsilon^2}\right]}$$

where, $\boldsymbol{T}$ is finite temperature and $\boldsymbol{f_0(\varepsilon) = 1/(e^{(\varepsilon-\mu_c)/T} + 1)}$ is the Fermi-Dirac distribution and $\boldsymbol{\varepsilon}$ is the energy. Equation 1 can be evaluated in the local limit of the random phase approximation (RPA) with finite $\boldsymbol{T}$ and finite relaxation time $\boldsymbol{\tau}$ [41-43].

(Equation-2)

$$\sigma(\omega) = \frac{2e^2T}{\pi\hbar}\frac{i}{\omega + i\tau^{-1}} log[2\, cosh(\mu_c/2k_B\, T] + \frac{e^2}{4\hbar}\left[H(\omega/2) + \frac{4i\omega}{\pi}\int_0^\infty d\varepsilon \frac{H(\varepsilon) - H(\omega/2)}{\omega^2 - 4\varepsilon^2}\right]$$

where $H(\varepsilon) = \sinh(\hbar\varepsilon/k_BT)\,/(\cosh(\,\mu_c/k_B\,T) + \cosh(\,\hbar\varepsilon/k_B\,T))$ and k_B is the Boltzmann constant. The first term in Equation 2 is known as intra-band, and the second term corresponds to inter-and scattering process. At low frequencies, Drude response for intra-band transitions dominates when $1/\tau = 0$ [35].

(Equation-3)

$$\sigma(\omega)_{intra} = i\frac{2e^2T}{\pi\hbar\omega} log[2\, cosh(\mu_c/2\, k_B\, T]$$

At high frequencies, inter-band transitions dominates with $\delta = 0$ and in terms of step function $H(\omega/2) = \theta(\omega - 2\mu_c)$ for $\mu_c \gg k_BT$.

(Equation-4)

$$\sigma(\omega)_{inter} = \frac{e^2}{4\hbar}\left[\theta(\hbar\omega - 2\mu_c) - \frac{i}{\pi}\log\left|\frac{\hbar\omega - 2\mu_c}{\hbar\omega + 2\mu_c}\right|\right]$$

Inter-band transitions occur when $\hbar\omega \geq 2\mu_c$ at short wavelengths. In order to analyze graphene plasmons, intra-band transitions are considered, $\hbar\omega < 2\mu_c$, in mid- and far-IR frequency ranges. The dispersion relation for surface plasmons can be derived from Dyadic Green's functions for a surface model of graphene by considering incoming TE and TM plane waves under boundary conditions [36]. In the presence of high doping, TM mode (related with intra-band transitions of conductivity) dominates such that the dispersion relation is described by $k_{SP} \approx i\omega(\epsilon + 1)/4\pi\sigma$ [43].

The Drude formula is inserted to the surface plasmon dispersion relation, which yields $k_{SP} \approx (\hbar^2/4e^2\mu_c)(\epsilon + 1)\omega(\omega + i\tau^{-1})$, i.e., the corresponding resonance wavelength is $(\lambda_{SP}/\lambda_0) \approx (\mu_c/\hbar\omega)(4\alpha/(\epsilon + 1))$, where $\alpha = (1/4\pi\epsilon_0)(e^2/\hbar c)$ is the fine structure constant, ϵ_0 is the permittivity of the free space, and c is the speed of light in vacuum.

RESULTS

We investigate the dependence of the optical behavior of UT-shaped graphene antennas on geometrical and other material parameters by FDTD simulations (Lumerical Solutions Inc.) [44]. The antenna system supports multi-band spectral response similarly to its plasmonic nanoparticle meta-material analog [45]. The geometrical parameters play an important role in the spectral position of the plasmonic resonances (observed as transmission minima) and provide a fine-tuning mechanism of spectral responses. The

schematics of UT-shaped graphene is presented in Figure 1, where the geometrical device parameters are H (height), L (length), w (rod width), s (distance between U- and T- antennas) and P is the period of the antenna array. The graphene structure stands on a (silicon nitride) SiN substrate. Normally incident light source impinges on the graphene substrate, polarized along the long edge of the antennas as depicted in the figure. In our numerical analyses, the intra-band conductivity of graphene at low frequencies is modeled with Drude approximation at $T = 300\,K$ and scattering length $\Gamma = 1/2\tau$, where the total conductivity is studied at the entire far-IR frequency range.

Along $\boldsymbol{x}$- and $\boldsymbol{y}$-axes, periodic boundary condition is used and along the direction of the incident light ($\boldsymbol{z}$), perfectly matched layer is used. As shown in Figure 2A, the graphene antenna arrays supports 3 distinct transmission resonances at $\boldsymbol{\lambda_1 = 24\,\mu m}$, $\boldsymbol{\lambda_2 = 37\,\mu m}$, $\boldsymbol{\lambda_3 = 53\,\mu m}$. In Figure 2B-2D, total electric field intensities ($|\boldsymbol{E}|^2$) at air-graphene interface are presented for the resonances. The first (at $\boldsymbol{\lambda_1}$) and second (at $\boldsymbol{\lambda_2}$) modes are originated from the constituting U-shaped graphene antenna, while the third one (at $\boldsymbol{\lambda_3}$) is associated with the T-shaped structure. The electromagnetic field intensity enhancement calculated on the top surface of the graphene is due to the excitation of localized surface plasmons, which show a dipolar character and induces strong nearfield enhancements particularly on the edge of the constituting U- and T-shaped antennas.

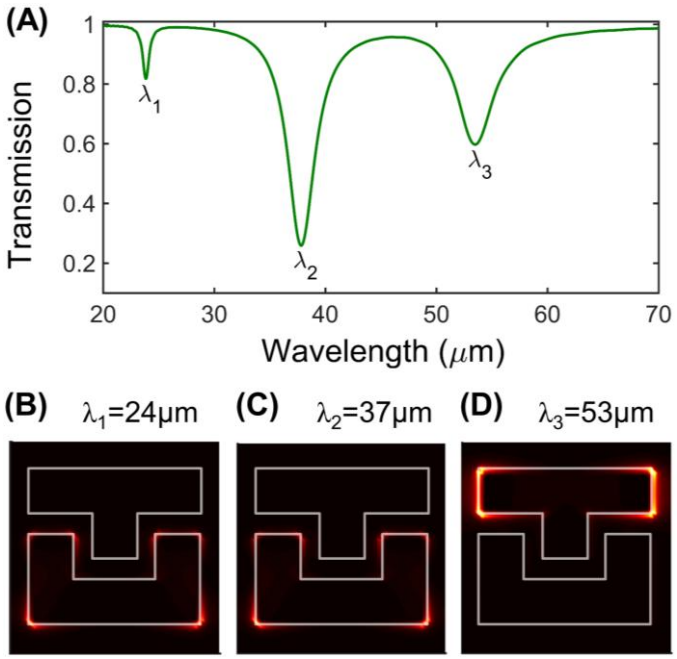

Figure 2. (a) Transmission spectrum of UT-shaped graphene antenna arrays, where $\boldsymbol{\mu_c = 0.4\,eV}$, $\boldsymbol{N = 1}$ and $\boldsymbol{\tau = 0.5\,ps}$. Corresponding device parameters are $\boldsymbol{H = 0.2\,\mu m}$, $\boldsymbol{L = 0.4\,\mu m}$, $\boldsymbol{s = 0.05\,\mu m}$, $\boldsymbol{w = 0.1\,\mu m}$ and $\boldsymbol{d = 0.07\,\mu m}$. The total electric field intensities, $|\mathbf{E}|^2$, are shown for the 3 distinct transmission resonances at (b) $\boldsymbol{\lambda_1 = 24\,\mu m}$, (c) $\boldsymbol{\lambda_2 = 37\,\mu m}$, and (d) $\boldsymbol{\lambda_3 = 53\,\mu m}$.

First, we investigate the dependence of the transmission spectrum of the UT-shaped graphene antenna on the geometrical device parameters. In Figure 3A, $\boldsymbol{H}$ (height) is varied while the other parameters are kept constant. The modes at $\boldsymbol{\lambda_1 = 24\ \mu m}$ and $\boldsymbol{\lambda_2 = 37\ \mu m}$ shift to longer wavelengths with $\boldsymbol{H}$ (Figure 3B). This is due to the fact that, for these modes, the local electromagnetic fields concentrate along the arms of the constituting U-shaped antenna, i.e., varying $\boldsymbol{H}$ strongly affects the position of these modes. On the other hand, the mode at $\boldsymbol{\lambda_3 = 53\ \mu m}$ shows unpredictable spectral variations as the local electromagnetic fields associated with this mode concentrate at antenna elements which are not characterized by $\boldsymbol{H}$ variations, i.e., we observe blue and red shifts for $\boldsymbol{H = 0.3\ \mu m}$ and $\boldsymbol{H = 0.25\ \mu m}$, respectively.

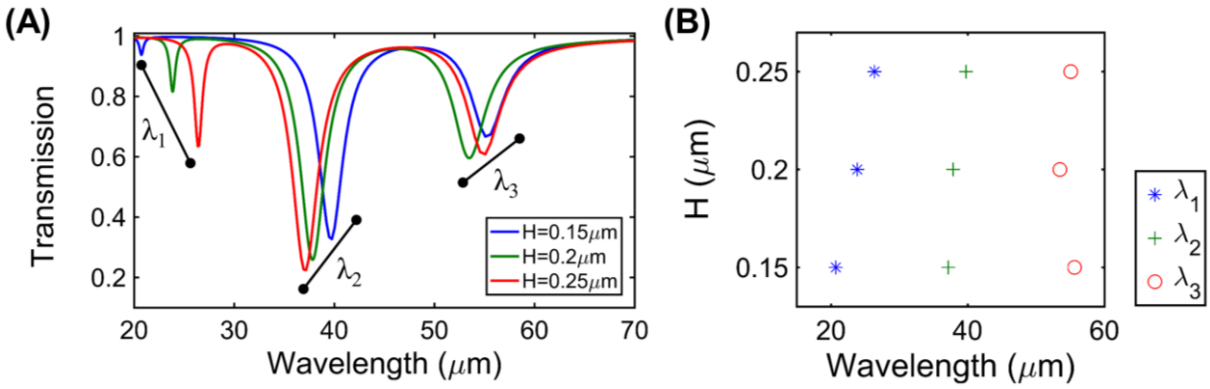

Figure 3. (a) Transmission spectrum of UT-shaped graphene antenna arrays with $H = 0.15\ \mu m$, $H = 0.2\ \mu m$, $H = 0.25\ \mu m$, where $\mu_c = 0.4\ eV$, $N = 1$, $\tau = 0.5\ ps$, $L = 0.4\ \mu m$, $s = 0.05\ \mu m$, $w = 0.1\ \mu m$, $d = 0.07\ \mu m$. (b) Spectral position vs. H for 3 distinct resonances at λ_1, λ_2 and λ_3.

In Figure 4A, we show the dependence of the transmission resonances on $\boldsymbol{L}$ (length). Analog to Fabry-Perot resonator for nano-antenna configurations, dipolar resonances appear at integer multiples of resonant wavelength which is linearly proportional to the length, along the polarization direction [46-48]. Similarly for the UT-shaped graphene antenna, the increase in the length shifts the resonances wavelength of all 3 modes to longer wavelengths as $\boldsymbol{L}$ variation alters the lengths of rod which belong to the constituting U- and T-shaped antennas along the polarization direction (Figure 4A). Figure 4B, showing the spectral position of each transmission resonance for different $\boldsymbol{L}$ values, clearly demonstrates this linear relation. More importantly, the field localization at the edge of the rods for the mode at $\boldsymbol{\lambda_3}$ is stronger than those of the modes at $\boldsymbol{\lambda_1}$, $\boldsymbol{\lambda_2}$ such that the shift in the transmission resonance corresponding this mode is larger compared to the later ones.

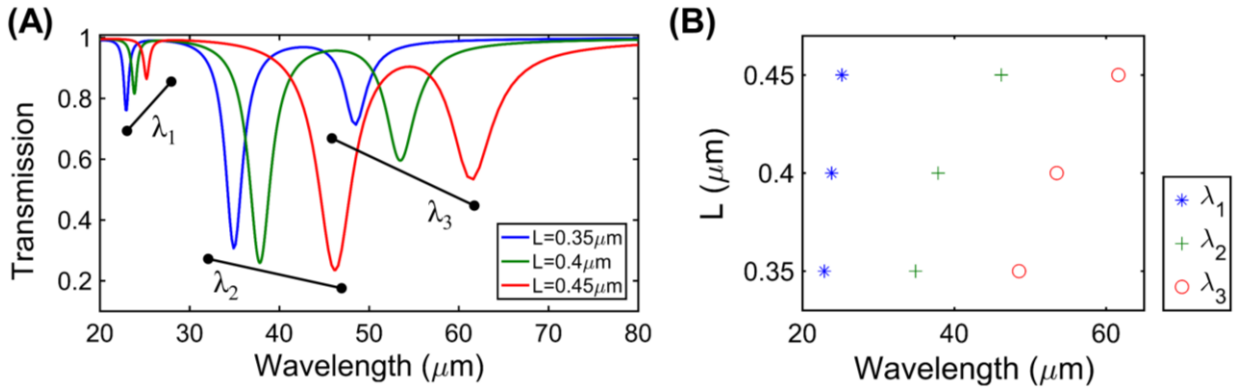

Figure 4. (a) Transmission spectrum of UT-shaped graphene antenna arrays with $L = 0.35\ \mu m$, $L = 0.4\ \mu m$, $L = 0.45\ \mu m$, where $\mu_c = 0.4\ eV$, $N = 1$, $\tau = 0.5\ ps$, $H = 0.2\ \mu m$, $s = 0.05\ \mu m$, $w = 0.1\ \mu m$, $d = 0.07\ \mu m$. (b) Spectral position vs. L for 3 distinct resonances at λ_1, λ_2 and λ_3.

In Figure 5, we investigate the effect of the distance between constituting U- and T-shaped graphene antennas ($\boldsymbol{s}$) on the transmission resonances supported by the UT-shaped antenna. We observe that the spectral position of the mode at $\boldsymbol{\lambda_1}$ remains unchanged for different values of $\boldsymbol{s = 0.03\mu m}$, $\boldsymbol{0.05\mu m}$ and $\boldsymbol{0.07\mu m}$, while its amplitude varies. On the other hand, the one at $\boldsymbol{\lambda_2}$ experiences a slight red-shift, while its amplitude does not vary. Unlike the other modes, the mode at $\boldsymbol{\lambda_3}$ shows both blue- and red-shifts for different $\boldsymbol{s}$ values, suggesting a critical distance between the constituting antennas in the composite structure, which plays the dominant role for the interference between these elements. Here, the mode at $\boldsymbol{\lambda_3}$ experiences a large spectral shift compared to the others as the field localization for this mode is much stronger at the antenna edges of the constituting T-shaped antenna, where $\boldsymbol{s}$ variation mainly alters.

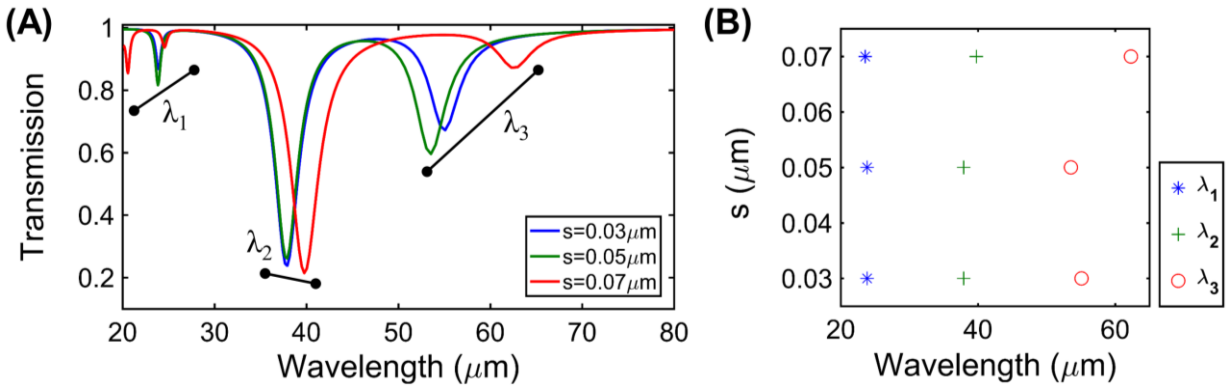

Figure 5. (a) Transmission spectrum of UT-shaped graphene antenna arrays with $s = 0.03\ \mu m$, $s = 0.05\ \mu m$, $s = 0.07\ \mu m$, where $\mu_c = 0.4\ eV$, $N = 1$, $\tau = 0.5\ ps$, $H = 0.2\ \mu m$, $L = 0.4\ \mu m$, $w = 0.1\ \mu m$, $d = 0.07\ \mu m$. (b) Spectral position vs. s for 3 distinct resonances at λ_1, λ_2 and λ_3.

In Figure 6A, we investigate the dependence of the transmission resonances supported by the UT-shaped graphene antenna array on the width of the antenna ($\boldsymbol{w}$). All three resonant modes show similar

spectral behavior for larger width, i.e., they shift to shorter wavelengths and their transmission amplitude increases.

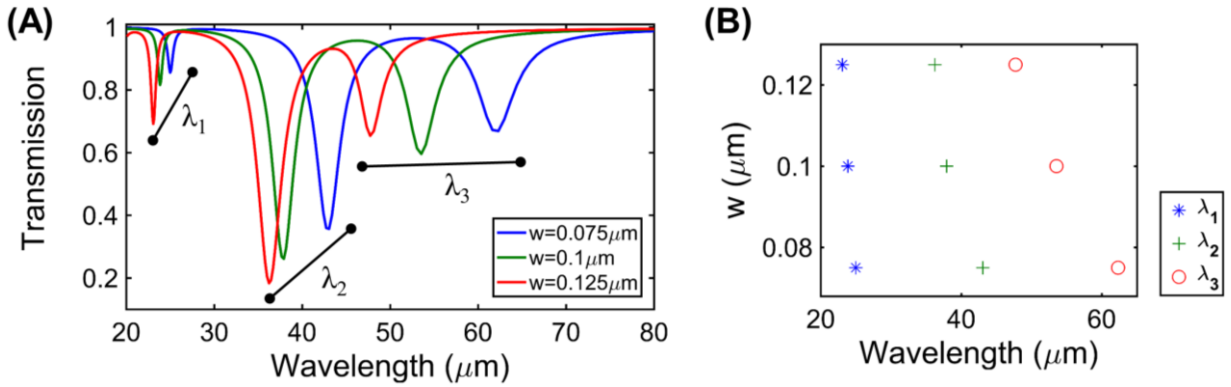

Figure 6. (a) Transmission spectrum of UT-shaped graphene antenna arrays with $w = 0.075\ \mu m$, $w = 0.1\ \mu m$, $w = 0.125\ \mu m$, where $\mu_c = 0.4\ eV$, $N = 1$, $\tau = 0.5\ ps$, $H = 0.2\ \mu m$, $L = 0.4\ \mu m$, $s = 0.05\ \mu m$, $d = 0.07\ \mu m$. (b) Spectral position vs. w for 3 distinct resonances at λ_1, λ_2 and λ_3.

In Figure 7 at all three resonant modes at $\boldsymbol{\lambda_1 = 24\ \mu m, \lambda_2 = 37\ \mu m, \lambda_3 = 53 \mu m}$, for larger periods, transmission resonances shifts to shorter wavelengths. This is due to the decrease in the coupling between each UT-shaped antenna in the array as the separation between them increases [6]. We also observe a reduction in the transmission for larger periodicity. One reason behind this again the reduction is in the weakening of the coupling strength between each UT-shaped antennas. The second reason that as the period increases, the ratio between the number of photon impinges on the UT-shaped antenna and the that of the incident photon increases.

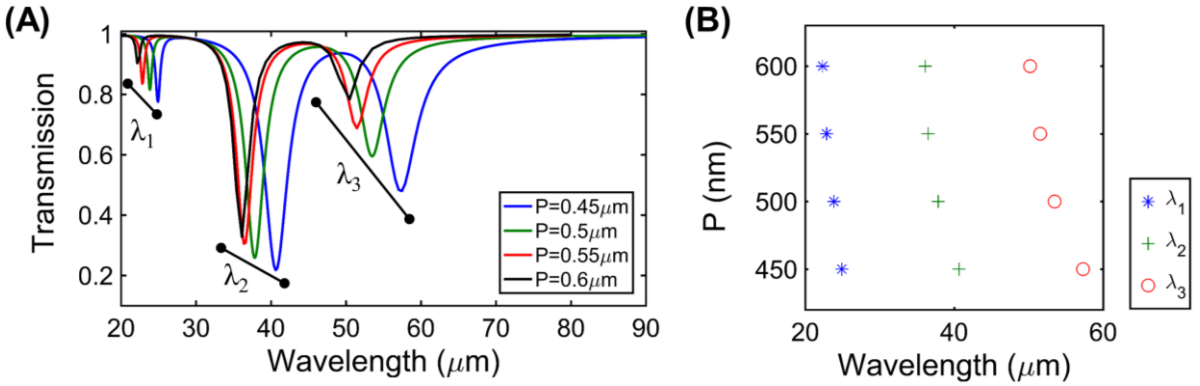

Figure 7. (a) Transmission spectrum of UT-shaped graphene antenna arrays with $P = 0.45\ \mu m$, $P = 0.5\ \mu m$, $P = 0.55\ \mu m$, $P = 0.6\ \mu m$, where $\mu_c = 0.4\ eV$, $N = 1$, $\tau = 0.5\ ps$, $H = 0.2\ \mu m$, $L = 0.4\ \mu m$, $w = 0.1\ \mu m$ $s = 0.05\ \mu m$, $d = 0.07\ \mu m$. (b) Spectral position vs. P for 3 distinct resonances at λ_1, λ_2 and λ_3.

The chemical potential, μ_c, for electrons refers to a Fermi level ($\boldsymbol{\mu_c \approx E_F \approx \hbar v_f k_f}$, where $\boldsymbol{k_f}$ is the diameter of Fermi sphere) and Drude model at low frequencies is $\boldsymbol{\sigma(\omega) = (e^2 \mu_c / \pi \hbar^2)(i/\omega + i\tau^{-1})}$ with $\boldsymbol{\mu_c \gg k_B T}$. From the definition of the Drude model, larger $\boldsymbol{\mu_c}$ induces an increase in the conductivity. Inserting $\boldsymbol{\sigma(\omega)}$ to the definition of the plasmonic wavelength, $\boldsymbol{\lambda_{sp} = 2\eta\omega Re[k_{sp}/k_0]}$, we can obtain the resonant wavelength as a function of Fermi energy [49-51]:

(Equation-5)

$$\boldsymbol{\lambda_{sp} = \frac{2\pi\hbar c}{e}\sqrt{\frac{\eta\varepsilon_0(\varepsilon_{r1}+\varepsilon_{r2})\omega}{E_F}}}$$

where $\boldsymbol{\eta}$ is dimensionless constant (function of $\boldsymbol{E_F}$), which represents the electrodynamic response of the graphene plasmonic structure. Knowing the fact stated above $\boldsymbol{\mu_c \approx E}$, transmission resonances shift toward shorter wavelength (Figure 8). Furthermore as plasmonic oscillations increase with the number of carriers, transmission corresponding to these resonances increases.

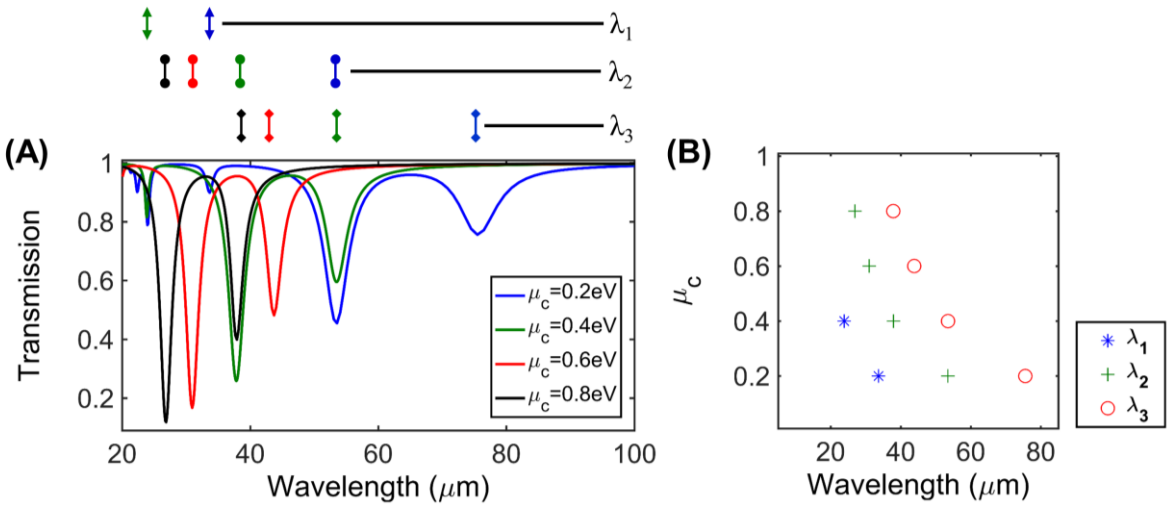

Figure 8. (a) Transmission spectrum of UT-shaped graphene antenna arrays with $\mu_c = 0.2\ eV$, $\mu_c = 0.4\ eV$, $\mu_c = 0.6\ eV$, $\mu_c = 0.8\ eV$, where $N = 1$, $\tau = 0.5\ ps$, $H = 0.2\ \mu m$, $L = 0.4\ \mu m$, $P = 0.5\ \mu m$, $w = 0.1\ \mu m$ $s = 0.05\ \mu m$, $d = 0.07\ \mu m$. (b) Spectral position vs. μ_c for 3 distinct resonances at λ_1, λ_2 and λ_3. For a constant $\tau = 0.5\ ps$, the carrier densities are 7.35x10^{12}, 1.47x10^{13}, 2.2x10^{13}, and 3x10^{13} cm^{-2} for $\mu_c = 0.2, 0.4, 0.6, and\ 0.8\ eV$, respectively.

In Figure 9, we investigate the effect of the number of graphene layer ($\boldsymbol{N}$) on the transmission spectra of the antenna system. The total optical conductivity can be evaluated by considering the individual layers as $\boldsymbol{N\sigma_T(\omega)}$ [52], where $\boldsymbol{\sigma_T(\omega)}$ is the total dynamical conductivity. For larger number of layers, number of electrons that contributes to the plasmonic oscillations increases. Thus, the corresponding transmission spectra shifts to shorter wavelengths from $\boldsymbol{N = 1}$ to $\boldsymbol{N = 4}$. After $\boldsymbol{N = 4}$, for the spectral window of interest, multi-band behavior is no longer observed.

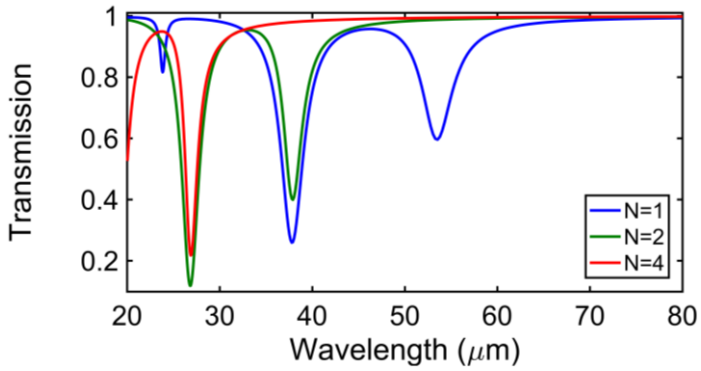

Figure 9. Transmission spectrum of UT-shaped graphene antenna arrays with $N = 1$, $N = 2$, $N = 4$, where $\mu_c = 0.4\ eV$, $\tau = 0.5\ ps$, $H = 0.2\ \mu m$, $L = 0.4\ \mu m$, $P = 0.5\ \mu m$, $w = 0.1\ \mu m$ $s = 0.05\ \mu m$, $d = 0.07\ \mu m$.

The carrier mobility and chemical potential are strongly related to the relaxation time of electrons in graphene, e.g., $\boldsymbol{\tau = \mu_c\ \mu / e v_f^2}$, where $\boldsymbol{\mu}$ can be tuned by changing carrier concentration through doping with another molecule. In Figure 10A, transmission spectrum of the UT-shaped graphene antenna array is presented for different $\boldsymbol{\tau}$ values, while other parameters are kept constant. The resonance peak remains constant with $\boldsymbol{\tau}$ for all transmission resonances. On the other hand, the amplitude of the transmission peak increases with larger number of carriers that contributes to the plasmonic oscillations.

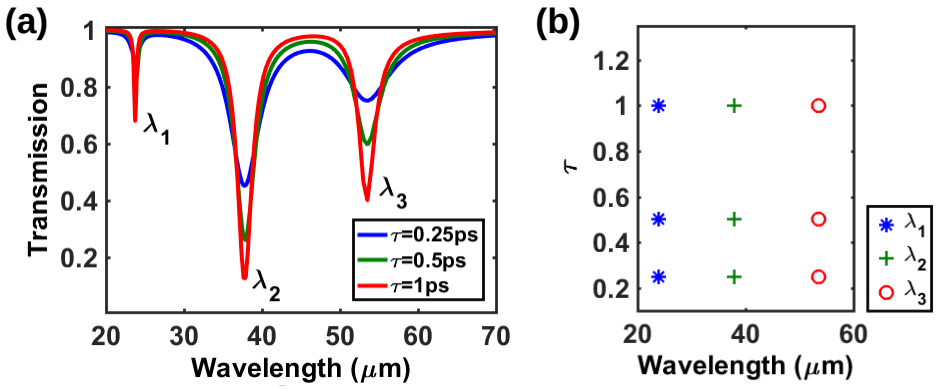

Figure 10. (a) Transmission spectrum of UT-shaped graphene antenna arrays with $\tau = 0.25\ ps$, $\tau = 0.5\ ps$, $\tau = 1\ ps$, where $\mu_c = 0.4\ eV$, $N = 1$, $H = 0.2\ \mu m$, $L = 0.4\ \mu m$, $P = 0.5\ \mu m$, $w = 0.1\ \mu m$ $s = 0.05\ \mu m$, $d = 0.07\ \mu m$. (b) Spectral position vs. τ for 3 distinct resonances at λ_1, λ_2 and λ_3. For a given chemical potential of $\mu_c = 0.4\ and\ \tau = 0.25, 05,$ and 1ps, the carrier densities are 7.35x10^{12}, 1.47 x10^{13}, and 3 x10^{13} cm^{-2}, respectively.

CONCLUSION

In conclusion, we introduce a multi-band UT-shaped graphene antenna arrays. The antenna platform supports three resonances, where their peak wavelength depends on the geometry of the structure, suggesting a fine-tuning mechanism of optical responses. The physical origin of this dependence is investigated by nearfield calculations. We also investigate the effect of chemical potential, number of graphene layers and relaxation time on the transmission spectrum of the UT-shaped graphene antenna.

ACKNOWLEDGES

Yasa Ekşioğlu acknowledges the support of Istanbul Kemerburgaz University Scientific Research Foundation project No: PB2016-I-012.

REFERENCES

1. Stern EA, Ferrell RA (1960) Surface plasma oscillations of a degenerate electron gas. Phys Rev 120:130–136

2. Ozbay E (2006) Plasmonics: merging photonics and electronics at nanoscale dimensions. Science 311:189–193

3. Maier SA (2007) Plasmonics: fundamentals and applications. Springer, New York

4. Kneipp K, Wang Y, Kneipp H, Perelman LT, Itzkan I, Dasari RR, Field MS (1997) Single molecule detection using surface-enhanced Raman scattering (SERS). Phys Rev Lett 78:1667–1670

5. Kundu J, Le F, Nordlander P, Halas NJ (2008) Surface enhanced infrared absorption (SEIRA) spectroscopy on nanoshell aggregate substrates. Chem Phys Lett 452:115–119

6. Adato R, Yanik AA, Amsden JJ, Kaplan DL, Omenetto FG, Hong MK, Erramili S, Altug H (2009) Ultra-sensitive vibrational spectroscopy of proteinmonolayers with plasmonic nanoantenna arrays. Proc Natl Acad Sci U S A 106:19227–19232

7. Kabashin AV, Evans P, Pastkovsky S, Hendren W, Wurtz GA, Atkinson R, Pollard R, Podolskiy VA, Zayats AV (2009) Plasmonic nanorod metamaterials for biosensing. Nat Mater 8:867–871

8. Artar A, Yanik AA, Altug H (2009) Fabry–Pérot nanocavities in multilayered plasmonic crystals for enhanced biosensing. Appl Phys Lett 95:051105

9. Atwater HA, Polman A (2010) Plasmonics for Improved Photovoltaic Devices. Nat Mater 9: 205–213.

10. Grigorenko AN, Polini M, Novoselov KS (2012) Graphene plasmonics. Nat Photonics 6:749-758

11. Low T, Avouris P (2014) Graphene plasmonics for terahertz to midinfrared applications. ACS Nano 8:1086-1101

12. Garcia de Abajo FJ (2014) Graphene Plasmonics: Challenges and Opportunities. ACS Photon 1:35-152

13. Geim AK, Novoselov KS (2007) The rise of graphene. Nature Materials 6:183–191.

14. Bonaccorso F, Sun Z, Hasan T, Ferrari AC (2010) Graphene photonics and optoelectronics. Nature Photonics 4:611 - 622

15. Song J, Zhang L, Xue Y, Yang Q, Wu S, Xia F, Zhang C, Zhong YL, Zhang Y, Teng J, Premaratne M, Qiu CW, Bao Q (2016) Efficient excitation of multiple plasmonic modes on three-dimensional graphene: an unexplored dimension. ACS Photonics 3:1986-1992

16. Liu PQ, Valmorra F, Maissen C, Faist J (2015) Electrically tunable graphene anti-dot array terahertz plasmonic crystals exhibiting multi-band resonances. Optica 2: 135-140

17. Jablan M, Buljan H, Soljačić M (2009) Plasmonics in graphene at infrared frequencies. Phys Rev B 80:245435

18. Gao W, Shi G, Jin Z, Shu J, Zhang Q, Vajtai R, Ajayan PM, Kono J, Xu Q (2013) Excitation and active control of propagating surface plasmon polaritons in graphene. Nano Lett. 13:3698 -3702

19. Yan H, Low T, Zhu W, Wu Y, Freitag M, Li X, Guinea F, Avouris P, Xia F (2013) Damping pathways of mid-infrared plasmons in graphene nanostructures. Nat Photonics 7:394-399

20. Gao W, Shu J, Qiu C, Xu Q (2012) Excitation of plasmonic waves in graphene by guided-mode resonances. ACS Nano 6*:* 7806-7813

21. Nene P, Strait J, Chan WM, Manolatou C, Kevek JW, Tiwari S, McEuen PL, Rana F (2013) Graphene Micro- and Nano-Plasmonics. QTh1B.2 CLEO:2013 OSA

22. Li HJ, Zhai X, Sun B, Huang ZR, Wang LL (2015) A Graphene-Based Bandwidth-Tunable Mid-Infrared Ultra-Broadband Plasmonic Filter. Plasmonics 10:765–771

23. Said FA, Menon PS, Nawi MN, Md Zain AR, Jalar A, Majlis BY (2016) Copper-graphene SPR-based biosensor for urea Detection. IEEE-ICSE Proc doi:10.1109/SMELEC.2016.7573642

24. Lee JK, Kim H (2016) Mid-infrared plasmonic tuning via nanogap control in periodic multilayer graphene nanoribbons. Optical Materials 54:22–25

25. Xia F, Mueller T, Lin YM, Valdes-Garcia A, Avouris P (2009) Ultrafast graphene photodetector. Nature NanoTech 4:839-843

26. Freitag M, Low T, Zhu W, Yan H, Xia F, Avouris P (2013) Photocurrent in graphene harnessed by tunable intrinsic plasmons. Nat Comm 4:1951

27. Cai X, Sushkov AB, Jadidi MM, Nyakiti LO, Myers-Ward RL, Gaskill DK, Murphy TE, Fuhrer MS, Drew HD (2015) Plasmon-enhanced terahertz photodetection in graphene. Nano Lett 15: 4295-4302

28. Ju L, Geng B, Horng J, Girit C, Martin M, Hao Z, Bechtel HA, Liang X, Zettl A, Shen YR, Wang F, (2011) Graphene plasmonics for tunable terahertz metamaterials. Nat Nanotechnol 6:630-634

29. Sensale-Rodriguez B, Yan R, Zhu M, Jena D, Liu L, Xing HG (2012) Efficient terahertz electro-absorption modulation employing graphene plasmonic structures. Appl Phys Lett 101:261115

30. Otsuji T, Popov V, Ryzhii V (2014) Active graphene plasmonics for terahertz device applications. J Phys D Appl Phys 47: 094006

31. Brar VW, Sherrott MC, Jang MS, Kim S, Kim L, Choi M, Sweatlock LA, Atwater HA (2015) Electronic modulation of infrared radiation in graphene plasmonic resonators. Nat Comm 6: 7032

32. Wang X, Zhi L, Mullen K (2008) Transparent, Conductive graphene electrodes for dye-sensitized solar cells. Nano Letters 8:323–327.

33. Rodrigo D, Limaj O, Janner D, Etezadi D, García de Abajo F J, Pruneri V, Altug H (2015) Mid-infrared plasmonic biosensing with graphene. Science Reports 349: 165-168

34. Zhao Y, Hu X, Guanxiong C, Xuanru Z, Ziqi T, Junhua C, Rodney SR, Yanwu Z, Yalin L, (2013) Infrared biosensors based on graphene plasmonics: modeling. Physical Chemistry Chem Phys15:17118-17125

35. Falkovsky L, Pershoguba S (2007) Optical far-infrared properties of a graphene monolayer and multilayer. Physical Review B 76:1–4

36. Hanson GW (2008) Dyadic Green's functions for an anisotropic, nonlocal model of biased graphene. IEEE Transactions on Antennas Propagation 56:747–757

37. Falkovsky LA (2008) Optical properties of graphene. Journal of Physics: Conference Series 129:012004

38. Gan CH, Chu HS, and Li EP (2012) Synthesis of highly confined surface plasmon modes with doped graphene sheets in the mid infrared and terahertz frequencies. Phys. Rev B 85:125431

39. Ke S, Wang B, Huang H, Long H, Wang K, Lu P (2015) Plasmonic absorption enhancement in periodic cross-shaped graphene arrays. Opt Express 23:8888-8900

40. Jablan M, Buljan H, Soljačić M (2009) Plasmonics in graphene at infrared frequencies. Phys Rev B 80: 245435.

41. Wunsch B, Stauber T, Sols F, Guinea F (2006) Dynamical polarization of graphene at finite doping. New J Phys 8: 318

42. Hwang EH, S DS (2007) Dielectric function, screening, and plasmons in two-dimensional graphene. Phys Rev B 75: 205418

43. Koppens FH, Chang DE, de Abajo FJG (2011) Graphene Plasmonics: A Platform for Strong Light Matter Interactions. Nano Lett 11: 3370–3377

44. Finite-difference-time-domain package, Lumerical FDTD Solutions (2014) [Online]. Available: www.lumerical.com

45. Cetin AE, Turkmen M, Aksu S, Altug H (2012) Nanoparticle-Based Metamaterials as Multiband Plasmonic Resonator Antennas. IEEE Transactions on Nano Technology 11:208-212

46. Novotny L (2007) Effective Wavelength Scaling for Optical Antennas. Phys Rev Lett 98:266802

47. Liberman V, Adato R, Jeys TH, Saar BG, Erramilli S, Altug H (2012) Rational design and optimization of plasmonic nanoarrays for surface enhanced infrared spectroscopy. Opt Express 20:11953-11967
48. Cubukcu E, Capasso F (2009) Optical nanorod antennas as dispersive one-dimensional Fabry–Pérot resonators for surface plasmons. Appl Phys Lett 95: 201101
49. Krasavin AV, Zayats AV (2008) Three-dimensional numerical modeling of photonic integration with dielectric-loaded SPP waveguides. Phys Rev B 78:045425
50. Holmgaard T, Bozhevolnyi SI (2007) Theoretical analysis of dielectric-loaded surface plasmon-polariton waveguides. Phys Rev B 75:245405
51. Wu L, Chu HS, Koh WS, and Li EP (2010) Highly sensitive graphene biosensors based on surface plasmon resonance Opt. Express 18:14395-14400
52. Chu HS, Choon HG (2013) Active plasmonic switching at mid-infrared wavelengths with graphene ribbon arrays. Appl Phys Lett 102: 231107